Magnetospheric Constellation and Tomography Mission Concept

R. E. Ergun[1*], D. E. Larson[1], T. Phan[1], J. P. McFadden[1], C. W. Carlson[1], I. Roth[1], G. T. Delory[1], S. Bale[1], V. Angelopoulos[1], R. J. Strangeway[2], C. T. Russell[2], J. Raeder[2], P. A. Bernhardt[3], J. -L. Bougeret[4], R. Manning[4], J. Wygant[5], K. Goetz[5], R. Benson[6], J. Green[6], U. S. Inan[7], T. Bell[7], S. Fuselier[8], G. Paschmann[9], R. Nakamura[9]

Abstract. We describe the basic principles, instrumentation, and feasibility of a multi-satellite mission that combines *in situ* observations of plasma and electromagnetic fields with radio tomography imaging. We show that a 16-satellite radio tomography experiment can produce two-dimensional images of plasma density in the earth's magnetosphere at sufficient spatial (1/2 R_E) and temporal (~10 s) resolution to address key problems of magnetospheric physics. The same mission can incorporate electron and ion analyzers, magnetometers, and electric field instruments on the same spacecraft. We suggest that the large-scale images are more valuable when combined with *in situ* observations, supporting an unambiguous interpretation of the *in situ* data and an investigation of the interdependence of small- and large-scale plasma processes.

1. Introduction

Magnetospheric research over the past several decades has demonstrated the basic paradigm that the earth's magnetosphere is "open" [*Dungey*, 1961]. The interaction between the solar wind and magnetosphere results with energy and mass transfer across magnetic field lines and into the earth's magnetosphere proper. Magnetic flux is eroded from the day-side magnetosphere and stored in the magnetotail. A plasma sheet appears between the two lobes of the magnetotail where energy is stored and episodically released. The polar cusp is a major region of plasma entry into the magnetosphere and the ionosphere. The key to understanding magnetospheric processes lies in the critical regions: the bow shock, the magnetopause, the plasma sheet, and the cusp.

Past magnetospheric investigations gathered *in situ* observations of magnetospheric plasma, solar wind plasma, and their electromagnetic fields. These data have been the primary means for studying the complex plasma interactions that occur in the critical boundary regions such as the bow shock, the magnetopause [e.g. *Russell*, 1995], the central plasma sheet [*Baker et al.*, 1996, and references therein], and the auroral zone. These data also are the basis of statistical models of the magnetosphere.

There are, however, many open questions on the global nature of magnetospheric processes which cannot be answered with current data. These questions include (1) the spatial character and temporal properties of reconnection and associated plasma entry [e.g. *Sonnerup et al.*, 1995; *Paschmann et al.*, 1979], (2) the evolution of the plasma sheet, dipolarization region and their relationship with a near-earth neutral [*Baker et al.*, 1996], the relationship between plasma entry in the cusp regions and the state of the subsolar reconnection region [*Fuselier et al.*, 1997] and, (4) role of solar wind energy input at the lower-latitude boundary layer [*Phan et al.*, 1997]. These open questions illustrate the need for multi-point measurements of plasma and electromagnetic fields.

Performing additional experimental investigations with single-point measurements, as has been done in the past, will not rapidly advance the answers to these open questions. Magnetospheric boundaries are in constant motion making single-point observations difficult to interpret. What is needed are experimental investigations that provide concurrent measurements of plasma parameters over an extended region of the magnetosphere. Multi-point observations would resolve the ambiguity of space and time and the interdependence of small-scale plasma phenomena and large-scale magnetospheric processes could be investigated.

There are several approaches that one can use to achieve multi-point observations. In this article, we put forth a mission concept which combines *in situ* observations from a moderate number of spacecraft with remote sensing that can make large-scale images of the magnetospheric plasma density [*Ergun et al.*, 1988a]. The images are made concurrently with, and at the same location as, the *in situ* observations. With large-scale imaging, the *in situ* observations may be interpreted unequivocally. We discuss the basic principles, instrumentation, and feasibility of a 16-satellite mission which includes *in situ* observations and radio tomography imaging.

2. Scientific Goals

The primary scientific goal of a magnetospheric constellation and tomography mission is to investigate processes that govern energy flow and plasma entry into the magnetosphere, and release energy during magnetic substorms. These are some of the most important processes in magnetospheric physics which include plasma entry via reconnection, diffusion, and impulsive penetration, and the substorm process. Although *in-situ* observations have made remarkable advances, *in-situ* plasma measurements in context with global imaging are required to achieve closure. Specifically, the following important and controversial questions can be addressed:

Plasma Entry:

- What is the large-scale spatial and temporal nature of reconnection at the subsolar magnetopause? Is it steady state or bursty? Is it patchy or continuous? Is it driven or explosive? Are there multiple reconnection lines?
- Is there diffusive entry or impulsive penetration along the subsolar and flank magnetopause and, if so, how does it depend on the Interplanetary Magnetic Field (IMF)?
- What are the structure and plasma transport processes in the exterior cusp, and what controls reconnection sites and rates?

Substorm Processes and Plasma Sheet Formation:

- What is the relative timing of the substorm process? Which process initiates a substorm?

[1]Space Sciences Laboratory, University of California, Berkeley, CA
*Currently at Brown University, Providence, RI
[2]University of California, Los Angeles, CA
[3]Naval Research Laboratory, Washington, DC
[4]Observatoire De Paris, Meudon, France
[5]University of Minnesota, Minneapolis, MN
[6]NASA Goddard Space Flight Center, Greenbelt, MD
[7]Stanford University, Stanford, CA
[8]Lockheed Martin, Palo Alto, CA
[9]Max-Planck-Institut Fur Extraterreestrische Physik, Garching

Science Closure and Enabling Technologies for Constellation Class Missions, edited by V. Angelopoulos and P. V. Panetta, pp. 29-35, UC Berkeley, Calif., 1998.

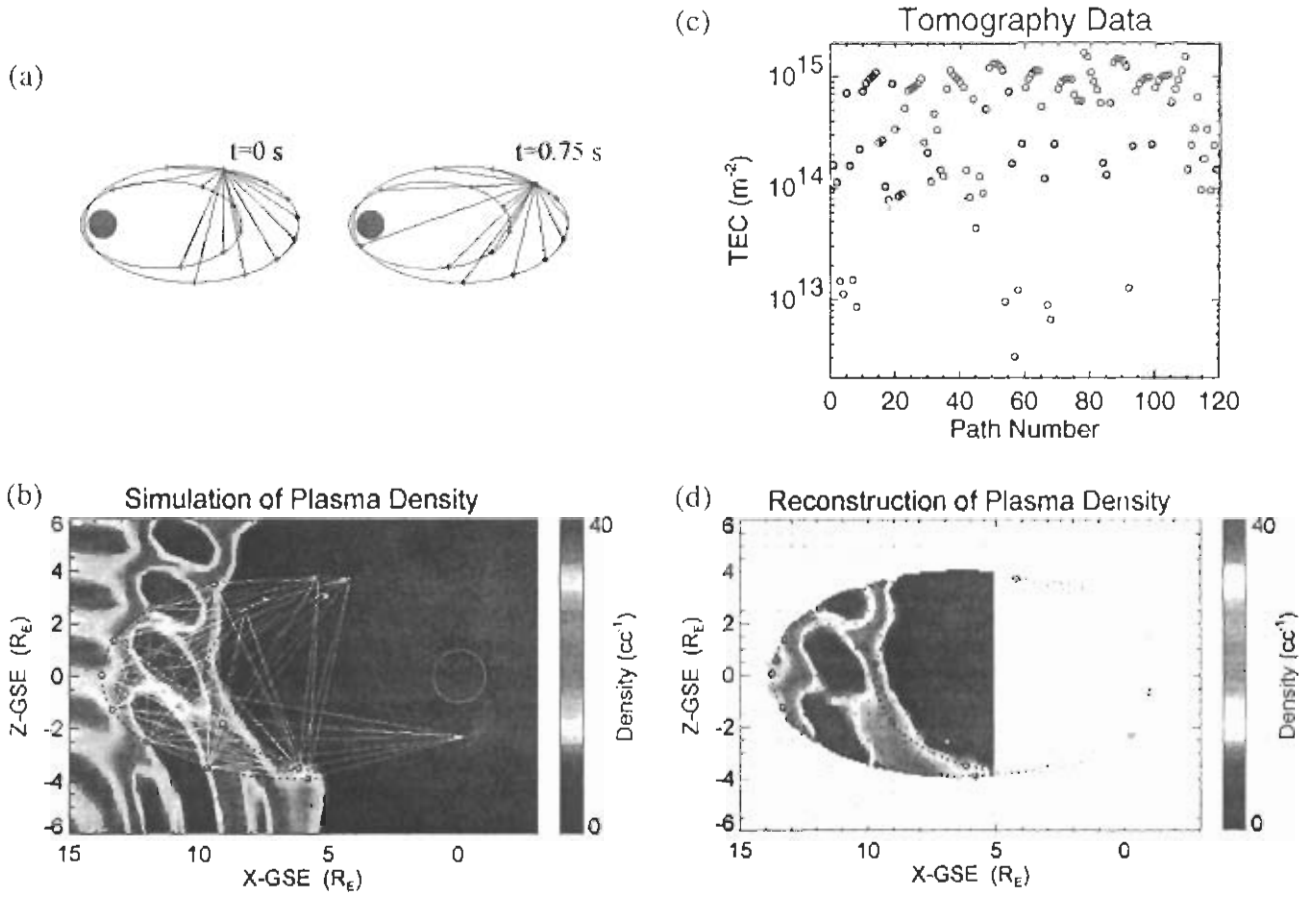

Figure 1. Radio tomography imaging. (a) Each spacecraft transmits a pair of coherently-phased radio signals that is received by all other spacecraft. The transmissions are for 0.4 s, every 0.75 s. The entire cycle takes 12 s. (b) From the transmissions, the total electron count (TEC) is determined. There are 120 ray paths between 16 spacecraft. This panel shows a 2-dimensional cut of electron density of the sub-solar magnetosheath through the GSM *XZ* plane based on a 3-dimensional MHD model [*Raeder et al.*, 1997]. A 25% oscillation at 2 R_E wavelength has been added.The orbits, instantaneous positions, and ray paths between sixteen satellites are superimposed. (c) The 120 TEC values and 16 local density measurements for the basis of the image. (d) The TEC values from a tomographic cycle are inverted to form the density image. The image has high spatial resolution where the TEC line density is highest, ~ 1/2 R_E. The high spatial resolution region is at X ~ 7 R_E to 14 R_E and Z ~ -3 R_E to 3 R_E.

- How does the plasma sheet form? What are the relative contributions from the low-latitude boundary layer, the mantle, the aurora, and the polar wind?

Additional Questions. These include:

- Short, large-amplitude magnetic structures as building blocks for quasi-parallel shocks.
- The presence/absence of a slow-mode standing wave upstream of the magnetopause.
- The formation and consequences of hot flow anomalies.

All of the above phenomena involve large-scale processes in the Earth's subsolar region, magnetotail, or cusp region. The magnetosheath, a region of enhanced density, extends from the magnetopause, typically ~10 R_E, to the bow shock, typically ~13 R_E, as do the most interesting regions of the cusp. The plasma sheet extends from ~8 R_E to > 20 R_E, with thickness that varies from ~8 R_E during quiet times to ~1 R_E just prior to substorm onset. The dipolarization process is believed to begin inside of ~10 R_E and expand tailward [*Ohtani et al.*, 1992], while near-earth neutral line formation is believed to occur between ~20 R_E and ~30 R_E [*Nagai et al.*, 1998]. An experimental investigation needs to cover a large region with sufficient spatial resolution to address the important questions in magnetospheric physics. Observations must include particle distributions and electromagnetic fields.

The experiment that we put forth uses radio tomography to image the plasma density over a large region, and multi-point in situ observations to measure particle distributions and electromagnetic fields. To answer the above scientific questions, one needs sufficient spatial resolution and time resolution. Flux transfer events, for example, are believed to be ~1 to 2 R_E moving at ~2 R_E per minute along the magnetopause. The depletion layer next to the MP in a layer typically thicker than ~0.5 R_E [*Zwan and Wolf*, 1976; *Anderson and Fuselier*, 1993]. Plasma sheet thicknesses need to be resolved down to ~1 R_E. The required spatial resolution is ~0.5 R_E. The constant motion (up to ~300 km/s) of magnetospheric boundary layers requires that images, at 0.5 R_E resolution, need to be made on time scales such that the motion is less than 0.5 R_E during the imaging period. This period is ~10 s.

3. Required Observations

The large-scale density images will provide the context for *in situ* observations. Full 3-D electron and ion distributions are needed to determine the energy flux, plasma density, pressure, and plasma flow.

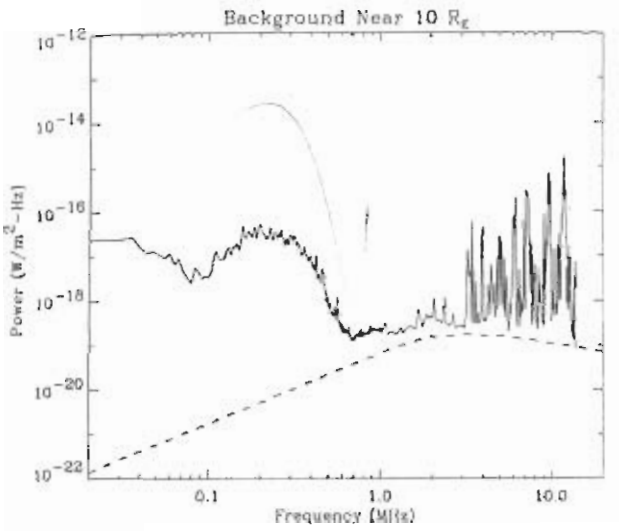

Figure 2. The expected wave electric field background in the near-earth magnetotail [*Ergun et al.*, 1998a]. The solid line represents average spectra from the Wind WAVES instrument between 8 R_E and 12 R_E [*Bougeret et al.*, 1995]. The dashed line is the cosmic background [*Novaco and Brown*, 1978]. The dotted line is the estimated auroral kilometric radiation level during a magnetic substorm based on FAST observations [*Ergun et al.*, 1998c]. The rectangles indicate the expected wave power from 2 R_E (top of rectangle) to 12.5 R_E (bottom of rectangles) assuming 20 W radiated power (left rectangle) and 50 W radiated power (right rectangle) and a 100 Hz bandwidth. The signal to noise ratio is ~20 dB, and can be improved to ~30 dB by averaging over a 0.1 second period.

and to analyze the stability and free energy in the plasma. The moments (density, velocity, energy flux) need to be quantitatively accurate. Previous work has demonstrated that the energy range from ~4 eV to 40 keV most often dominate the moments of the particle distributions. There occasionally are times that central plasma sheet distributions have substantial ion populations > 40 keV.

Magnetic fields reveal the basic structures and boundaries of the of the magnetosphere. Accurate magnetic field vectors are required to determine magnetic pressure and directions. Field strengths in the 7 R_E to 14 R_E magnetosphere vary from a few nT to a few 100 nT. Electric fields are required to provide large-scale potentials, plasma flow velocities (when ion energies exceed 40 keV or when flow speeds are below the thermal speeds), detect electric field spatial structures, and determine the modes and level of plasma turbulence.

4. Orbits

The 16 satellites are equally phased in two different polar orbits. Figures 1, "2", 3, and 4 show orbits during various phases. The orbits were designed to optimize *in situ* observations, satisfy the requirement for 0.5 R_E tomographic images, and satisfy spacecraft communications and power requirements. Six spacecraft will be in the inner most of the two orbits (1.43 x 9.75 R_E), which skims the subsolar magnetopause and cuts through one of the most dynamic region of the central plasma sheet. The outer orbit (1.1 x 13.75 R_E) has ten satellites which break through the bow shock into the solar wind. For typical solar wind conditions, at least one spacecraft will monitor the solar wind. The spacecraft in the solar wind will be immediately upstream of the region being studied, measuring the solar wind parameters. In the tail region, the inner and outer orbits will be in ideal locations to determine the direction and properties of fast flows and magnetic field dipolarization.

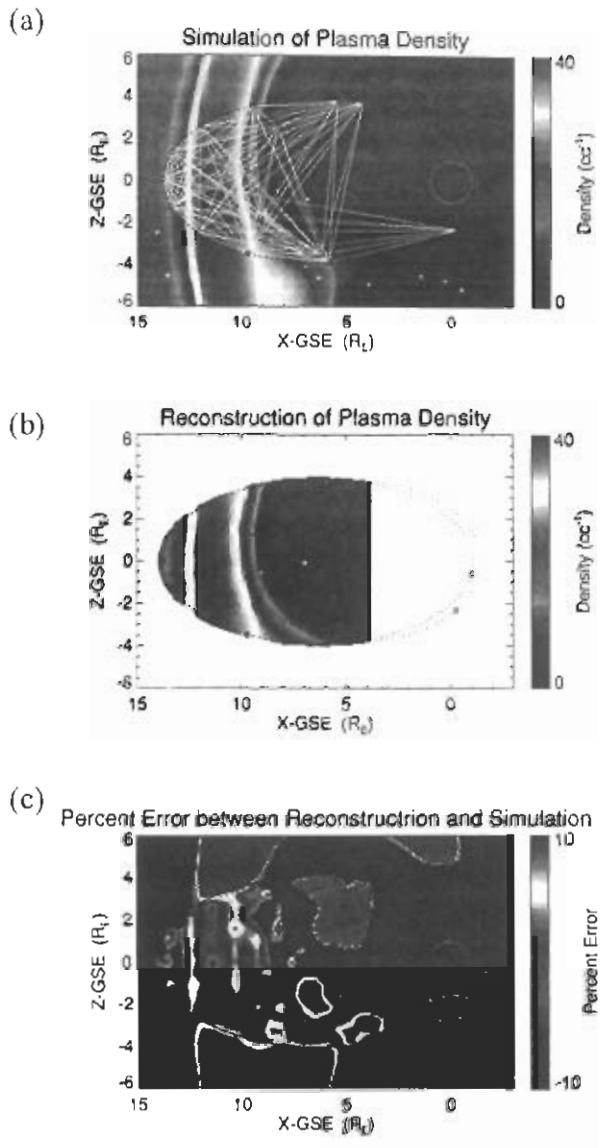

Figure 3. The top panel (a) shows a 2-dimensional cut of electron density of the sub-solar magnetosheath through the GSM *XZ* plane based on a 3-dimensional MHD model [*Raeder et al.*, 1997]. The orbits, instantaneous positions, and ray paths between sixteen satellites are superimposed. The middle panel (b) shows the reconstructed density based on the 120 simulated total electron count (TEC) measurements and 16 local electron density measurements. The spacecraft positions are indicated with diamonds and the pixel centers with points. (c) The error between the original and reconstructed image. The error is smallest where the ray path concentration is highest.

Tomographic imaging requires that spacecraft are coplanar within 1/2 R_E. The two orbits are designed to have identical precession rates (argument of perigee and right ascension), so small perturbations (in

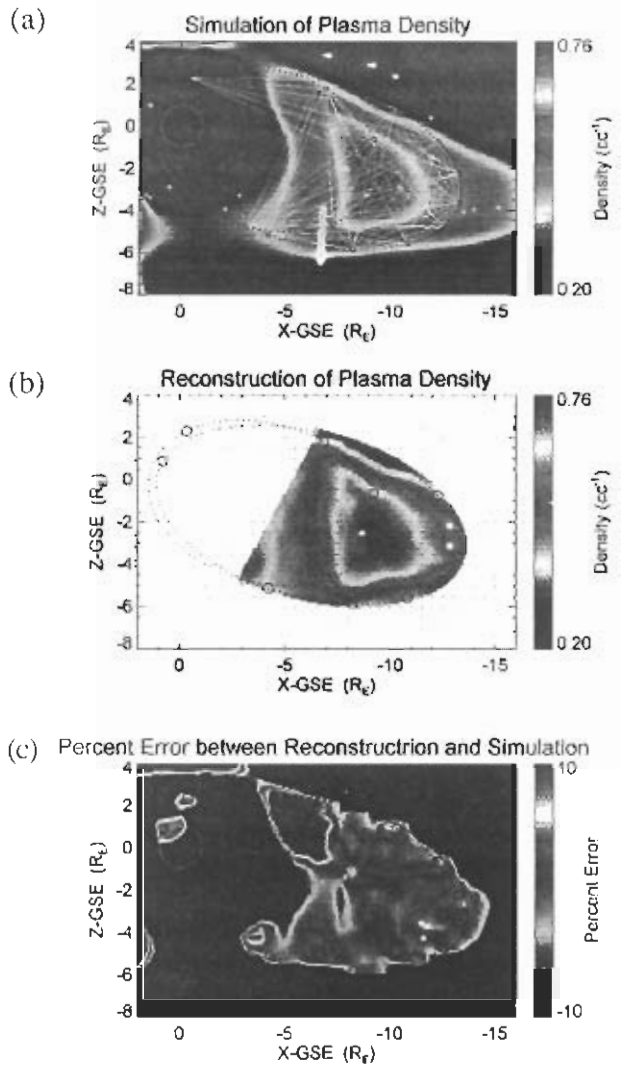

Figure 4. A demonstration of tomographic imaging in the near-earth plasma sheet. The display has the same format as Figure 3; the color scales have been adjusted to fit the local plasma densities.

inclination, for example) will not cause large dispersions. Solar and lunar perturbations have been thoroughly examined, and will not cause major dispersions. They will raise perigee. To maintain spacecraft phasing, orbital adjustments will be needed < 2 times per year.

5. Radio Tomography Imaging

Radio tomography imaging uses well-established radio science techniques and computed tomography to form images of plasma density. It works as follows. The spacecraft transmit, in turn, coherently phased pairs of discrete radio frequency signals to be received by all other satellites (Figure 1). The phase difference between the signals yields an accurate measurement of the total electron count (TEC). There are 120 column density measurements (along with 120 redundant measurements that can be used for consistency checking) that can be inverted to produce an image of the region encompassed by the satellites (Figure 1d). The tomographic cycle takes ~12 s with each satellite transmitting, in turn, 0.4 s in a ~0.75 s window. The spatial resolution can be as fine as ~$1/2\ R_E$ for the given orbit configuration. Measurements

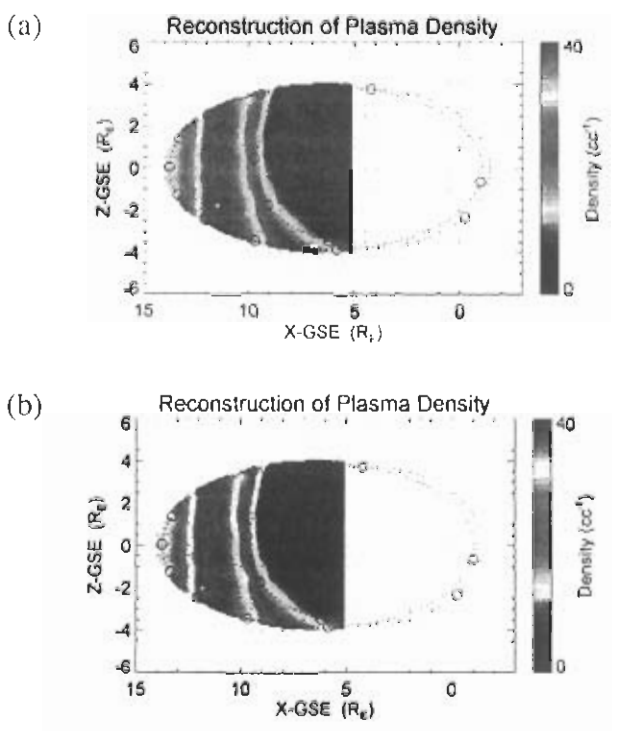

Figure 5. The affect of random errors in the data. Random errors of 2% and 5% were introduced into the simulated TEC measurements crating the images. Neither the image in the top plot (2% error) nor the image in the bottom plot (5% error) display false features. These images demonstrate that the tomographic inversion process is robust under measurement error in the TEC to ~ 5%.

of the ambient density are used to enhance the tomographic images.

This technique is considerably different than "magnetospheric sounding" employed by the *IMAGE* spacecraft. Because sounding detects echoes, the *IMAGE* spacecraft required long (>200 m) booms and high power. Radio tomography relies on a multi-spacecraft radio propagation experiment which requires considerably lower power, shorter booms, yet has much higher signal-to-noise ratios. Radio propagation experiments have conclusively demonstrated the ability to determine column electron densities, for example, the ISEE mission [*Celnikier et al.*, 1983].

5.1 Technique.

The technique used in radio propagation experiments is differential phase [*Leitinger*, 1994], which requires two phase coherent signals to propagate through the medium. The phase velocity of an electromagnetic wave ($w >> w_p, w_c$) in a plasma is:

$$v_\varphi \cong c(1 + \omega_p^2 / 2\omega^2 + \text{...h. o. t.}) \qquad (1)$$

where ω is the wave frequency, ω_p is the plasma frequency, and c is the speed of light. Higher order terms (h.o.t.) depend upon the wave polarization.

The expected phase difference ($\Delta\Phi_1$) between two signals with frequencies ω_1 and ω_{ref}, with respect to ω_1 is, to lowest order [*Ergun et al.*, 1998]:

$$\Delta\Phi_1 \cong \left(\frac{\omega_1 e^2}{2\varepsilon_0 m_e c}\right)\left(\frac{1}{\omega_1^2} - \frac{1}{\omega_{ref}^2}\right)\int n dL \qquad (2)$$

where e and m are electron charge and mass, and n is the plasma den-

sity. To first order, the phase difference between the two signals is directly proportional to the TEC ($\int ndL$).

$\Delta\Phi_1$ can be greater than 2π, in which case one needs to resolve the 2π ambiguity. This can be accomplished by shifting or modulating the probing frequencies. Since $\Delta\Phi_1$ is proportional to $1/\omega_1$, a small change in ω_1 will yield the derivative (ω_{ref} is the 3rd harmonic). Basically, a 1% shift in ω_1 leads to a -1% shift in $\Delta\Phi_1$, thus one measures, $\Delta\Phi_1/100$ from the modulation. The expected error is such that four levels of modulation are required to measure the extreme ranges of densities.

5.2 Broadcasting Frequencies.

For a given background, a lower-frequency system would have larger differential phase shift ($\Delta\Phi_1$) and, therefore, would allow a more accurate determination of the TEC. Lower-frequency systems, however, will experience higher second order disturbances and require much longer broadcasting antennae which may lead to technological limitations.

The background is also an important factor in choosing the radio science frequencies. Figure 2 displays the background at ~10 R_E in the equatorial plane. The dashed line represents the cosmic background noise [*Novaco and Brown*, 1978; *Bougeret*, 1984], the solid line is the average noise measured by the Wind spacecraft [*Bougeret et al.*, 1995] from 8 R_E to 12 R_E, and the dotted line represents auroral kilometric radiation (AKR) during an intense magnetic substorm at 10 R_E.

Strong emissions greater than ~3 MHz are narrow-band, man-made radio transmissions from earth. Below ~3 MHz, the ionosphere shields most of the man-made radio signals. This shielding should improve during solar maximum, during which, the ionospheric density increases. Below ~600 kHz, AKR and other naturally generated radio emissions dominate. Intense AKR will be emitted during interesting and perhaps critical states of the magnetosphere, so it is important that a radio science experiment can operate during the strongest AKR.

Inspection of Figure 2 clearly indicates that the 1 MHz to 3 MHz band has the lowest background, natural or man-made. There can be other natural emissions that are bursty in nature, such as solar type III radio bursts, that will temporarily increase the background.

5.3 Feasibility.

We examine a radio propagation experiment with a probing frequency of 1 MHz (fundamental) and a reference frequency of 3 MHz (3rd harmonic). The spacecraft have a typical separations of ~5×10^7 m (8 R_E). The plasma densities vary from ~0.01 cm^{-3}(104 m^{-3}) in the lobes of the magnetotail to ~100 cm^{-3} (108 m^{-3}) or more in a compressed magnetosheath. The expected TEC ranges from 5×10^{11} m^{-2} to 5×10^{15} m^{-2}.

The expected phase delay between two signals with frequencies of 1MHz and 3 MHz is (from equation 2):

$$\Delta\Phi_1 \cong 8.4\times10^{-13}\int ndL \quad \text{(radians)} \qquad (3)$$

where n (density) is in m^{-3} and L is in m.

The signal-to-noise (S/N) ratio determines the accuracy and feasibility of the TEC measurement. The noise at ~1 MHz has an intensity of ~1×10^{-19} W/(m^2-Hz) at ~10 R_E (Figure 2). The transmitters can achieve ~40 W radiated at the 3rd harmonic and ~12 W radiated at the fundamental. The power flux in the fundamental at the receiver, ~8 R_E (5×10^7 m) away, is ~3.6×10^{-16} W/m^2. The S/N ratio at the receiver would be ~24 dB (not accounting for losses/gains) when averaged over ~0.1 s. For this S/N ratio, the phase error would be ~2°. Under this error, the minimum average density that can be accurately (±1%) detected is <10^{-1} cm^{-3}.

In principle, the TEC measurement can be made at an precision approximately 5 times higher than required. In practice, there will be pattern losses (~1 dB) from the transmitter, losses/gains due to orientation of the receiving antennae (~3 dB offset by ~5 dB less noise due to solid angle coverage of a dipole), and occasionally a higher background. Even in the most unfavorable state, one still can determine of the TEC accurately enough to discern a 0.1 (±1%) cm^{-3} average density in as little as 0.1 s.

5.4 Tomographic Image Construction.

Tomographic techniques have been used in medical science for over a decade [*Lee and Wade*, 1985; *Kak and Slancy*, 1988]. The mathematical foundation was published by Radon as early as 1917 [*Deans*, 1983], and it was later shown that a broad class of images with a unique solution exist, as demonstrated through the back projection theorem [*Bracewell*, 1956]. Numerous techniques perform tomographic inversion [e.g. *Fougere*, 1995].

Tomographic inversion processes of plasma density using radio propagation experiments differs from those used in medical science. In medical imaging, the relation between fluxes of penetrating x-rays and the column density along the ray path is logarithmic. This relation limits the dynamic range of medical scans, but allows for detection of small variations. The measured phase shift ($\Delta\Phi_1$) in a radio propagation experiment is proportional to the TEC. Thus, radio tomography does not suffer from a limited dynamic range and is well-suited for investigating the magnetosphere. Furthermore, $\Delta\Phi_1$, a phase shift, can be accurately measured, so small variations also can be detected. On the other hand, medical scans typically have >10^4 column densities (or pixels) resulting in fine-scale, over-sampled images. The above mission will have at most 120 pixels and 16 in situ density measurements.

Under the a separate study [*Ergun et al.*, 1988a], we identified tow different techniques which can be applied to magnetospheric imaging. The most effective reconstruction technique that we tested was developed at UCB using an algorithm similar to the volumetric simultaneous iterative reconstruction technique [*Bernhardt et al.*, 1998 and references therein]. Figures 3 and 4 demonstrate the imaging technique, and the accuracy, in reconstructing the density profiles in the subsolar region and the magnetotail. Figure 5 demonstrates the error tolerance of the technique. Errors up to 5% in the TEC measurements do not notably alter the reconstruction. The correlation with the original image is > 90%. We demonstrated that at least two distinct reconstruction algorithms can properly reconstruct tomographic images of magnetospheric plasma to ~1/2 R_E resolution, and are tolerant of expected measurement errors.

6. Implementation

The *in situ* instrumentation and the radio tomography instrumentation are well known. The challenge is in implementing the 16 spacecraft mission that we put forth, obtaining orbits, acquiring data, and designing and constructing low-cost, light-weight satellites. In the section below, we briefly describe the results of a feasibility study of implementing a 16 spacecraft mission.

6.1 Orbit Attainment.

All 16 satellites can be placed in a 1.029 x 8.0 R_E staging orbit (13.5 hr period) by a single launch vehicle. The 16 satellites are held by a "dispenser" which releases the spacecraft in pairs, one pair every ~27 hr. The releases are programed to occur as the dispenser is approaching apogee, so the spacecraft can be immediately contacted.

Each of the spacecraft has a small hydrazine propulsion system for boost into final orbit and attitude maneuvers. The first maneuver adjusts the attitude and spin rate of the spacecraft for a perigee boost to 500 km. After the perigee boost, the apogees are boosted. The inner satellites require a second perigee boost to ~2700 km to keep the precession of the arguments of perigee identical to the outer satellites. Approximately 10 boosts are required to obtain the targeted orbits.

6.2 Operations.

A polar mission has a simple operation plan. The spacecraft acquire science data throughout the orbit and store it in a ~4 Gbit memory, sized for two orbits. The data volume is ~1.9 GBit per orbit for the outer spacecraft. Since the spacecraft are in polar orbits, the in-coming (northern) part of the perigee pass always has at least 20 minutes of viewing with a northern receiving station, and sufficient link margin for a 2.25 Mbit/s data rate. All of the stored data can be transmitted in ~14 minutes and each of the spacecraft can be contacted one at a time by a single ground station.

6.3 Spacecraft.

The spacecraft mass is described in Table 1. The mass analysis demonstrates that the spacecraft can be assembled at ~37 kg using "off-the-shelf" subsystems. The 16 spacecraft and dispenser are 672 kg, within the 750 kg vehicle capability. The spacecraft height (14") and diameter (32") are driven by the size of the hydrazine fuel tank and the required solar array area. The instruments and DPU are easily accommodated inside the spacecraft.

Table 1. Mass Summary (kg)

Component	Mass With 20% Reserve	Number	Total (kg)
Spacecraft	37.1 kg	16	594
Dispenser	78 kg		78
Total			672
Launch Capability			750
Margin		13%	78

6.4 Instruments.

The *in-situ* instruments have been flown on many missions and are well-understood, so we provide no description here. The instruments are summarized in Table 2.

7. Conclusions

Plasma and electromagnetic fields observations from single spacecraft of have provided the basis for investigating the magnetosphere. Many of the remaining questions cannot be answered with the current data set. We put forth an experimental approach that combines large-scale imaging with *in situ* observations. Under this approach, the data can be unambiguously interpreted as spatial or temporal phenomena and the interdependence of small-scale plasma phenomena and large-scale magnetospheric processes can be investigated.

We showed that radio tomography imaging can provide large-scale images of plasma density with sufficient resolution (~1/2 R_E, ~10s) to address key scientific questions of magnetospheric physics. There exist robust tomographic algorithms that are tolerant to errors. Empirical tests indicate that tomographic inversions require TEC observations with less than ~5% error. The frequency band between ~1 MHz and ~3 MHz provides an excellent domain of low-noise background. A satellite-borne radio science experiment can measure the TEC with the needed accuracy to image the plasma sheet and magnetosheath. A radio propagation experiment has been flown before on the *ISEE* spacecraft.

Table 2. Instrument summary.

Instrument	Measurement/ Function	Measurement Range	Recent Heritage
Ion Electrostatic Analyzer	Ion flux, T_i, v_i, and n_i. Solar wind n and v.	Energy Range: 4 eV - 40 keV	FAST Wind
Electron ESA	Electron flux, T_e, v_e, and n_e.	Energy range: 3 eV - 40 keV	FAST Wind
Fluxgate Magnetometer	Vector B. Attitude determination.	Range: ± 0.2 G. Sensitivity: 0.1nT	FAST Polar
Radio Science:			FAST
Antenna	Transmission/receiving. Electric Field.	Four 25 m wires.	Polar Cluster
Transmitter	Transmit 0.4 s pulses at 1 and 3 MHz.	12 W @ 1 MHz. 40 W @ 3 MHz.	Wind CRRES
Receiver	Total electron count. (Phase delay).	$5x10^{14}$ m-2 to $5x10^{15}$ m-2.	S3-3 ISEE1/2
Electric Field	2-axes E.	DC - 100 kHz. ±100 mV/m	FAST Polar
Radio Sounding	Local Density	10^{1} - 10^{5} cm^{-3}	ISIS

One of the challenges is to deploy 16 satellites into the appropriate orbits. Such operations have been done for the communications industry and, with the development of small-mass satellites, a radio tomography experiment can be carried out with a single launch vehicle. We have been able to describe orbits in which both in situ observations and radio tomography imaging can be performed by the same spacecraft. The combination of global imaging and multi-point, *in situ* observations can uniquely advance our understanding of the magnetosphere.

Acknowledgments. The authors thank the many engineers who contributed to the instrument designs. This research was conducted under NASA grant NAG5-3916.

References

Anderson, B. J., and S. A. Fuselier, Magnetic pulsations from 0.1 to 4.0 Hz and associated plasma properties in the Earth's subsolar magnetosheath and plasma depletion layer, *J. Geophys. Res.*, 98, 1461-1479, 1993.

Baker, D. N., T. I. Pulkkinen, V. Angelopoulos, W. Baumjohann, and R. L. McPherron, Neutral line model of substorms: past and present views, *J. Geophys. Res.*, 101, 12975-13010, 1996.

Bernhardt, P. A., R. P. McCoy, K. F. Dymond, J.M. Picone, R. R. Meier, F. Kamalabadi, D. M. Cotton, S. Charkrabarti, T. A. Cook, J. S. Vickers, A. W. Stephan, L. Kersley, S. E. Pryse, I. K. Walker, C. N. Mitchell, P. R. Straus, Helen, Na, C. Biswas, G. S. Bust, G. R. Kronschnabl, and T. D. Raymond, Two-dimensional mapping of the plasma density in the upper atmosphere with computerized ionospheric tomography, *Physics of Plasmas*, 5, 2010, 1998.

Bougeret, J. -L., J. Fainberg, and R. G. Stone, Interplanetary radio storms. I. Extension of solar active regions through the interplanetary medium, *Astron. Astrophys.*, 136, 255, 1984.

Bougeret, J. -L., Kaiser, M. L., Kellogg, P. J., Manning, R., Goetz, K, Monson, S. J., Monge, N., Friel, L., Meetre, C. A., Perche, C., Sitruk, L., and Hoang, S., WAVES: the radio and plasma wave investigation on the WIND spacecraft, *Space Sci. Rev.*, 71, 231, 1995.

Bracewell, R. N., Strip Integration in Radio Astronomy, *Aust. J. Physics*, 9, 198, 1956.

Celnikier, L.M., C. C. Harvey, R. Jegou, M. Kemp, and P. Moricet, A determination of the electron density fluctuation spectrum in the solar wind using the ISEE propagation experiment, *Astron. Astrophys.*, 126, 293-8, 1983.

Deans, S.R., *The Radon transform and some applications*, John Wiley, New York, 1983.

Dungey, J. W., Interplanetary magnetic field and the auroral zones, *Phys. Rev. Lett.*, 6, 47, 1961.

Ergun, R. E., et al., Feasibility of a multi-satellite investigation of the earth's magnetosphere with radio tomography, submitted, *J. Geophys. Res.*, 1998a.

Ergun, R. E., C. W. Carlson, J. P. McFadden, F. S. Mozer, G. T. Delory, W. Peria, C. C. Chaston, M. Temerin, R. Elphic, R. Strangeway, R, Pfaff, C. A. Cattell, D. Klumpar, E. Shelly, W. Peterson, E. Moebius, and L. Kistler, FAST Satellite Wave Observations in the AKR Source Region, *Geophys. Res. Lett.*, 25, 2061, 1998b.

Fougere, P. F., Ionospheric radio tomography using maximum entropy, *Radio Sci.*, 30, 429, 1995.

Fuselier, S.A., E.G. Shelley, W.K. Peterson, O.W. Lennartsson, H.L. Collin, J.F. Drake, A.G. Ghielmetti, H. Balsiger, J.L. Burch, A. Johnstone, H. Rosenbauer, and J.T. Steinberg, Bifurcated cusp ion signatures: evidence for re-reconnection? *Geophys. Res. Lett.*, 24, 1471-4, 1997.

Kak, A. C., and M. Slaney, *Principles of Computerized Tomographic Imaging*, IEEE Press, New York, 1988.

Lee, H., and G. Wade, *Imaging Technology*, IEEE Press, New York, 1986.

Leitinger, R., Data from orbiting navigation satellites for tomographic reconstruction, *Imaging Systems and Technology*, 5, 85, 1994

Nagai, T. et al, Structure and dynamics of magnetic reconnection for substorm onsets with Geotail observations, *J. Geophys. Res.*, 103, 4419, 1998.

Novaco, J.C. and L.W. Brown, Nonthermal galactic emission below 10 megahertz. *Astrophys. J.*, 221, 114-23, 1978.

Ohtani, S., S. Kokubun, and C. T. Russell, Radial expansion of the tail current disruption during substorms: A new approach to the substorm onset region, *J. Geophys. Res.*, 97, 3129-3136, 1992.

Paschmann, G., B. U. O. Sonnerup, I. Papamastorakis, N. Sckopke, G. Haerendel, S. J. Bame, J. R. Asbridge, J. T. Gosling, C. T. Russell, and R. C. Elphic, Plasma acceleration at the Earth's magnetopause: evidence for reconnection, *Nature*, 282, 243, 1979.

Phan, T. -D., D. Larson, J. McFadden, C. Carlson, M. Moyer, K.I. Paularena, M. McCarthy, G.K. Parks, H. Reme, T.R. Sanderson, and R.F. Lepping, Low-latitude dusk flank magnetosheath, magnetopause, and boundary layer for low magnetic shear: wind observations, *J. Geophys. Res.*, 102, 19883-95, 1997.

Raeder, J., J. Berchem, M. Ashour-Abdalla, L. A. Frank, W. R. Paterson, K. L. Ackerson, R. P. Lepping, S. Kokubun, T. Yamamoto, and S. A. Slavin, Boundary layer formation in the magnetotail: Geotail observations and comparisons with a global MHD model, *Geophys. Res. Lett.*, 24, 951, 1997.

Russell, C. T., in *Physics of the Magnetopause*, P. Song, B. U. O. Sonnerup, and M. F. Thomsen, editors. AGU, 1995.

Sonnerup, B. U. O., G. Paschmann, and T. -D. Phan, Fluid aspects of reconnection at the magnetopause: In situ observations, in *Physics of the Magnetopause*, AGU Monograph 90, 167, 1995.

Zwan, B. J. and R. A. Wolf, Depletion of solar wind plasma near a planetary boundary, *J. Geophys. Res.*, 81, 1636-48, 1976.

V. Angelopoulos, S. Bale, C. W. Carlson, G. T. Delory, R. E. Ergun, D. E. Larson, J. P. McFadden, T. Phan, I. Roth, Space Sciences Laboratory, University of California, Berkeley, CA 94720. (e-mail: vassilis; bale; cwc; ccc; gdelory; ree; davin; mcfadden; phan; illan@ssl.berkeley.edu)

J. Raeder, C. T. Russell, R. Strangeway, IGPP, University of California, Los Angeles, CA 90095. (e-mail: strange@igpp.ucla.edu)

P. A. Bernhardt, Naval Research Laboratory, Washington, DC.

J. -L. Bougeret, R. Manning, Observatoire De Paris, Meudon, France.

J. Wygant, K. Goetz, Tate Laboratory of Physics, University of Minnesota, Minneapolis, MN 55455. (e-mail: wygant@belka.spa.umn.edu)

R. Benson, J. Green, NASA Goddard Space Flight Center, Code 696, Greenbelt, MD 20771. (e-mail: rob.pfaff@gsfc.nasa.gov)

T. Bell, U. S. Inan, Stanford University, Stanford, CA.

S. Fuselier, Lockheed Palo Alto Research Lab., Palo Alto, CA 94304. (e-mail: sfuselier@agena.space.lookheed.com)

R. Nakamura, G. Paschmann, Max-Planck-Institut Fur Extraterreestrische Physik, Garching.